STALL FLUTTER EXPERIMENT IN A TRANSONIC OSCILLATING LINEAR CASCADE

D. R. Boldman, A. E. Buggele, and G. M. Michalson

National Aeronautics and Space Administration
Lewis Research Center
Cleveland, Ohio

ABSTRACT

The results of steady state and flutter experiments in a nine-blade oscillating linear cascade are presented. Two-dimensional biconvex airfoils were oscillated at reduced frequencies up to 0.5 based on semi-chord and a free stream Mach number of 0.80 to simulate transonic stall flutter in rotors. Steady-state periodicity was confirmed through end-wall pressure measurements, exit flow traverses, and flow visualization. The initial flow visualization results from flutter tests indicated that the oscillating shock on the airfoils lagged the airfoil motion by as much as 80 deg. These initial data exhibited an appreciable amount of scatter; however, a linear fit of the results indicated that the greatest shock phase lag occurred at a positive interblade phase angle. Photographs of the steady-state and unsteady flow fields reveal some of the features of the lambda shock wave on the suction surface of the airfoils.

E-918

NOMENCLATURE

C	chord
C_p	pressure coefficient
DEV	deviation, eq. (4)
f	airfoil oscillatory frequency
i	incidence angle
M	Mach number
$\mathcal{M}$	aerodynamic moment
P	static pressure
P_t	total pressure
R	gas constant
S	airfoil spacing
S_A	amplitude of airfoil displacement signal
t	time
T_t	total temperature
x	coordinate in chordwise direction
α	angle of attack
α_c	mean angle of attack
$\bar{\alpha}$	airfoil oscillatory amplitude
β	flow angle
γ	stagger angle
δ^o	deviation angle
θ_{TS}	test section setting angle
κ	airfoil setting angle
Φ_s	shock phase lag
ψ_p	probe setting angle
Ω	reduced frequency based on airfoil semi-chord
ω	angular frequency
$\bar{\omega}$	total pressure loss $\langle P_{t,1} - P_{t,2} \rangle / (P_{t,1} - \bar{P}_1)$

Subscripts

1	upstream condition
2	downstream condition
m	maximum
s	associated with shock wave
u	upper surface
l	lower surface

Superscripts

$\bar{}$	average value
*	critical value

INTRODUCTION

Flutter has been observed in turbomachinery since the advent of the first axial flow jet engines. This highly undesirable self-excited oscillation of the blades in fans and compressors is sustained through the extraction of energy from a moving airstream. Flutter can occur in several different operating regimes of the fan or compressor and can manifest itself in several different oscillatory modes. A good dicussion of these various types of flutter is given by Carta (1). Of all of these possible types of flutter, one of the least understood from a theoretical standpoint is transonic stall flutter. The purpose of the present investigation was to provide information that might serve in the development of new theories for the prediction of this type of flutter.

The results described in this paper are from exploratory experiments in a novel oscillating linear cascade which was developed with the primary goal of studying the aerodynamics of transonic stall flutter.

Emphasis was placed on the generation of realistic reduced frequencies by the simultaneous simulation of the oscillatory mode and frequency, geometric scale (blade chord), and free stream Mach number. Driven cascades, although not as common as classical steady state cascades, have been used in studies of other types of turbomachinery flutter, e.g., (2) to (4). In all cases, the airfoils were oscillated by a controlled external source designed to produce either a two-dimensional pitching or plunging motion to simulate a torsional or bending mode of flutter. By performing experiments in this way, the aerodynamic aspects can be separated from the structural aspects of flutter, and the results should be of value in the formulation of models for predicting the aerodynamic damping or stability of fan and compressor blading.

BACKGROUND

Transonic stall flutter occurs near the stall limit line of fans and compressors at speeds of perhaps 75 percent of the design speed. The principal mode of oscillation in this regime is a pitching or torsional mode. At a subsonic relative Mach number greater than about 0.7, the flow in the tip region of a rotor blade can locally exceed a Mach number of unity and a region of supersonic flow appears on the blade. The supersonic region is terminated by a normal shock wave and the flow again becomes subsonic. This type of flow field exhibits many of the features observed on an oscillating isolated airfoil as reported in (5), (6), and (7); however, in using the results to model the flow around a blade row, the "cascading" effect or influence of the adjacent blades must be taken into account. As the blades flutter, these regions of supersonic flow move over the blade so that the phase between the shock and blade motion is non-unity. Under certain conditions this shock wave motion can introduce an additional contribution to the fluctuating forces on the airfoil and thus influence the stability of the system (8). Therefore, an understanding of the shock wave dynamics becomes essential to the modeling of analyses for the prediction of transonic flutter.

The present paper focuses on this aspect of flutter through the use of flow visualization methods. Results are presented for steady state and unsteady experiments which were performed with nine biconvex airfoils operating at a free stream Mach number of 0.80. During the flutter experiments, the airfoils were oscillated to provide a pitching motion of 1.2 deg about the midchord axis at nominal frequencies of 160 to 550 Hz. The reduced frequency based on the airfoil semichord was nominally 0.5 at the 550 Hz condition. Results from the initial flow visualization experiments are presented for interblade phase angles of 0 and ± 90 deg. The above conditions are believed to be valid for the experimental modeling of the unsteady fluid dynamics associated with torsional stall flutter in fans and compressors.

DESCRIPTION OF CASCADE

Experimental Facility

An overall view of the transonic oscillating cascade is shown in Fig. 1. Room air entered the inlet contraction section and expanded through a 9.78-cm wide by 29.21-cm high test section into a diffuser and exhaust header having a nominal pressure of 3.0 N/cm. Flow rates were controlled by means of two valves located downstream of the diffuser. A partitioned (5 section) end-wall boundary layer bleed system located 2 chord lengths upstream of the airfoils was used to remove the boundary layer on each end wall and provide steady state blade-to-blade periodicity. The bleed passages consisted of perforated plates having an open area ratio of 22.5 percent and a hole diameter of 0.15 cm. The boundary layers on the upper and lower walls of the cascade were removed through slots between the tailboards and the walls. These boundary layer control systems are shown in Fig. 2.

During the flutter experiments the nine airfoils were oscillated in a pitching (torsional) motion about the midchord axes by a mechanical drive system powered by a 100 h.p. motor. The oscillatory or flutter frequency could be varied in a continuous manner by an eddy-current coupling between the motor and gearbox. The direction of rotation of the motor drive system was reversible so that the sign of the interblade phasing could readily be changed from positive to negative.

Airfoils

Nine two-dimensional, uncambered, biconvex airfoils with a chord of 7.62 cm and a span of 9.6 cm were installed as shown in Fig. 2. The airfoil radius of curvature was 27.4 cm, yielding a maximum thickness of 0.58 cm or a thickness-to-chord ratio of 0.076. This airfoil thickness provided the stiffness required to maintain a two-dimensional flutter mode at the highest oscillatory frequency of 550 Hz. The airfoils were supported by two trunnions with the centerline located at the midchord as shown in Fig. 3. The larger trunnion which was used to oscillate the airfoil had a diameter of 1.91 cm whereas the freely supported shaft had a diameter of 0.95 cm. Each airfoil and its trunnions were machined from a single piece of titanium containing 6 percent aluminum and 4 percent vanadium.

Test Section

The airfoils were mounted between end walls containing three 0.64-cm-thick mirrors on one side and three optical quality glass windows on the other side (refer to Fig. 2). These mirrors and windows comprised part of a Schlieren flow visualization system used to observe the flow field. Nonporous bronze alloy bushings containing two "O" rings and helical lubrication grooves were used to support the large trunnion. A similar bronze alloy bushing was lightly pressed into the glass window to provide support for the small trunnion.

The limitation in the region of flow visualization over the airfoil surface was governed by the large trunnion and the size of the corresponding hole in the mirror required to accommodate the small fillet at the airfoil-trunnion junction (Fig. 3). The diameter of this hole, which appears as a shadow in the Schlieren images, was 2.3 cm.

Airfoil Drive System

Electromagnetic and mechanical drive systems have been used for the torsional oscillation of airfoils in cascades as reported e.g., in (2) and (4), respectively. Electromagnetic drivers are capable of generating controlled high frequency oscillations (hundreds of Hz); however, the amplitude of the motion decreases with increasing frequency and/or increasing blade loading. Mechanical drive systems are normally used for low frequency operation (perhaps up to 100 Hz).

In the present investigation, it was desirable to maintain control of the oscillatory amplitude as well

as the frequency; therefore, a high-speed mechanical drive system was developed for this purpose. This system, which represents a modification of the drive mechanism design described in (7), consists of a series of nine female barrel cams attached to a common 50-cm diameter shaft as shown in Fig. 4. Each cam contained a 6-cycle, 1.27-cm-wide by 0.762-cm-deep sinusoidal groove machined in the surface. A close-coupled 7.62-cm long connecting arm and button follower transmitted 6 cycles of harmonic pitching motion for each revolution of the cam. The amplitude of the airfoil motion was 1.2 deg as dictated by the cam and follower geometry. Power from the motor drive system was transferred to the cam shaft by a 20.3-cm-wide endless belt consisting of layers of plastic-coated textile fabric, a polyester tension member, and a leather friction surface. The cams and followers were immersed in a multiviscosity 80W-140 high performance gear lubricant to minimize wear. With this system, each flutter test was arbitrarily limited to about 30 seconds with 15 to 20 seconds at the desired oscillatory frequency. With this operational mode, the cams and button followers incurred negligible wear.

INSTRUMENTATION

The instrumentation included 200 channels of pressures and temperatures from which the steady state cascade performance was established and an additional 40 channels of high pressure response data for the flutter tests. The steady state data were recorded through a system of micro-processors coupled to a dedicated minicomputer. The majority of pressures including end wall and airfoil static pressures and boundary layer bleed passage pressures were connected to a scanivalve system containing three 48-channel units scanning in parallel at a rate of 7 samples per second. The remainder of the pressures, used as reference values for the scanivalve system and for various traversing probes, were recorded through a system of signal conditioners and pressure transducers. Research and graphic CRT displays were used to expedite tuning of the cascade and provide on-line performance data. Off-line calculations of the detailed performance of the cascade were performed with an IBM 370 computer.

The temperatures in the cascade were essentially equal to the room temperature of 530 K. These temperatures were measured with chromel-alumel thermocouples having an ice reference-temperature junction.

The high frequency response measurements included the displacement and frequency of the vibrating airfoils and strain gauge signals on the cam follower arms. Airfoil displacement and oscillatory frequency were measured with an electro-optical displacement meter located outside the test section. This meter tracked a discontinuity of light reflected from the edge of the center airfoil and converted the optical image to an electron image. A servo loop controlled the position of the electron image in an aperture. The deflection current required to keep the image centered in the aperture was a measure of the airfoil angular displacement.

A network of two dual strain gauges were attached to opposite sides of the arm connecting the airfoil trunnion to the cam. Signals from a conventional full bridge circuit were recorded in order to determine the dynamic phase differences between the oscillating airfoils and verify the interblade phase angle which was preset by manually rotating each of the cams on the cam shaft.

All high response measurements were recorded on a frequency modulated (FM) magnetic tape recorder with a frequency response of 10 kHz. The output from the taped signals were analyzed on a Fast Fourier Transform (FFT) analyzer.

Flow visualization was accomplished by means of a double-pass Schlieren system shown in Fig. 5. The Schlieren images were photographed with a 16-mm high speed motion picture camera operating at about 5000 frames per second (or about 10 frames per cycle of airfoil motion). Steady state Schlieren photographs were obtained with a 70 mm camera and pulsed light source. The steady state images of the airfoil shock waves were used as a guide in verifying periodicity in the cascade. The motion pictures were used to determine the shock displacement along the airfoil and the phase lag relative to the motion of the airfoil.

As a part of the flow visualization study, a rapid-double-pulse laser holographic interferometer was used to determine the spanwise configuration of the shock wave during flutter. These tests were performed in a pilot facility (3-blade cascade) at the same nominal conditions as the present investigation. Typical results are described in the basis of holograms obtained by randomly pulsing the laser during the flutter experiments.

The periodicity in the cascade was determined by the uniformity of rows of upstream and downstream static pressures along the length of the cascade. The pressure taps were spaced 2.92 cm apart (one-half of the blade spacing) and were 1 and 2 chord lengths upstream and downstream of the airfoils, respectively.

Traversing probes were located at three tangential positions upstream of the airfoils for inlet flow angle and end wall boundary layer measurements. These measurements were obtained in the plane of the static pressure taps. A traversing probe, located downstream of the cascade, measured the local flow angle, and static and total pressures in the tangential direction.

GEOMETRIC PARAMETERS

The coordinate system and geometric parameters for the cascade are shown in Fig. 6. All of the tests were performed at a test section angle, θ_{TS}, of 30 deg and an angle of attack, α_o, of 7.0 deg. The resulting blade stagger angle, γ, was 53 deg. The solidity or chord-to-spacing ratio, C/S, was 1.3. Since the biconvex airfoils were uncambered, $i = \alpha$ and $\gamma = \kappa_1 = \kappa_2$.

INLET FLOW CONDITIONS

All of the flutter tests were performed at the same inlet flow velocity, V_1, of 258 m/s (M = 0.80). Although the cascade periodicity was optimized at this velocity, the periodicity did not change significantly over a range of about $180 < V_1 < 260$ m/s. The inlet Mach number and velocity were calculated from the end wall pressures and the stagnation pressure and temperature assuming isentropic flow conditions. The resulting expressions for $\gamma = 1.4$ are

$$M_1 = \left\{ 5 \left[\left(\frac{\bar{P}_1}{P_t} \right)^{-2/7} - 1 \right] \right\}^{1/2} \qquad (1)$$

$$V_1 = \left(1.4\ RT_t M_1^2\right)^{1/2} \Big/ \left(1 + \frac{M_1^2}{5}\right)^{-1/2} \qquad (2)$$

The static pressure $\bar{P}_1$ was the average value of a specified number of end wall pressures and was given by

$$\bar{P}_1 = \sum_{i=M1}^{N1} \frac{P_{1,i}}{N1 - M1 + 1} \qquad (3)$$

The limits M and N were selected to include the 11 pressures directly upstream of the 5 central airfoils in the cascade. The values of P_t and T_t were based on the room air conditions in the test cell.

RESULTS

The following discussion will consider the results of the steady state and flutter tests separately. An appreciable effort was dedicated to the steady state experiments which were required in order to establish periodicity in the cascade. This so-called "tuning" of the cascade was followed by the flutter experiments in which certain features of the shock dynamics were observed.

Steady State Performance

Distributions of the upstream and downstream static pressures are shown in Fig. 7 for the design conditions. The quality of these distributions was determined from the RMS deviation of pressure given by

$$DEV1 = \left\{ \sum_{i=M1}^{N1} \frac{(\bar{P}_1 - P_{1,i})^2}{N1 - M1 + 1} \right\}^{1/2} \qquad (4)$$

The lowest values of deviation (best uniformity) were nominally 0.7 kPa for both the upstream and downstream distributions based on the values of M and N given in Fig. 7. The maximum deviation from the average pressure was nominally 2 percent at each station. This corresponds to a velocity deviation of about 2.5 percent over the 5 central airfoils.

The upstream end wall boundary layers were measured at the three tangential stations (Fig. 6) with a dual-tube pitot probe referenced to the end-wall static pressure. With this probe, shown schematically in Fig. 8, both end-wall boundary layers could be measured in a single sweep. The total pressure distributions indicate a boundary layer thickness of about 1.0 cm corresponding to a total displacement thickness of two percent of the passage width. The similarity of the profiles at the three tangential stations was directly influenced by the end-wall bleed flows which were established by experimental iterative procedures.

The spanwise variation in inlet flow angle at the center of the cascade was measured with a self-nulling flow angle probe. The variation in angle was within 1 deg between the end walls and within 1 deg of the design inlet setting angle, θ_{TS}, as shown in Fig. 9.

Wake surveys were obtained with a traversing probe of the type shown in Fig. 6. The plane of the surveys was 0.33 chordlengths downstream of the trailing edge of the cascade. The measured pressures from this probe were converted to true values based on calibration data obtained in a free jet. The exit flow angle, β_2, was also obtained from this probe through a similar calibration procedure which is described in (9). The surveys were made over several airfoils to observe the flow periodicity and over a single passage to permit more detail in the wake. Values of the deviation angle, δ^o, and total pressure loss, $\bar{\omega}$, were obtained from the mass-averged values of β_2 and $P_{t,2}$.

The total pressure distributions across the three center airfoils are shown in Fig. 10. Corresponding distributions of the total pressure across the wake from the center airfoil are presented in Fig. 11. Based on these two distributions, the total pressure loss parameter, $\bar{\omega}$, was 0.0286, and the deviation angle, δ^o, was 1.7 deg. These values of δ^o and $\bar{\omega}$ are generally consistent with the values reported in (10) for similar uncambered airfoils.

The chordwise distributions of pressure coefficient, C_p, on the center airfoil are shown in Fig. 12 for Mach numbers of 0.55, 0.67, 0.80 (design conditions), and 0.86. These distributions reveal the evolution of transonic flow (region above C_p^*) and the pronounced rise in pressure resulting from the formation of a lambda-type shock wave as the Mach number is increased. The results for the design Mach number of 0.80 indicate that a region of supersonic flow extends over a distance of about 12 percent of the chord (Fig. 12c).

Steady state Schlieren images of the design flow are shown in Fig. 13. The photographs clearly reveal the lambda-shock at the leading edge of the airfoils and a high degree of periodicity in the cascade. The position of the shock is also consistent with the C_p-distribution shown in Fig. 12c, i.e., it is located about 12 percent of the chordlength from the leading edge. The two photographs in Fig. 13 were obtained at the same flow conditions; however, the image in Fig. 13a was intentionally de-focused to provide higher contrast. The photograph in Fig. 13b was taken with a bicolor filter which replaced the knife edge in the Schlieren system.

Tests with Oscillating Airfoils

The airfoils were oscillated in simple harmonic motion to provide information on the phase between the shock and airfoil motion. This motion can be described by the following equation:

$$\alpha = \alpha_o - \bar{\alpha} \cos \omega t \qquad (5)$$

where the amplitude, $\bar{\alpha}$, was 1.2 deg and the mean angle of attack, α_o, was 7.0 deg. High speed motion pictures of the Schlieren images at nominal frequencies of 160 to 550 Hz. These frequencies yielded reduced frequencies ranging from 0.15 to 0.51 where the reduced frequency is

$$\Omega = \frac{\omega C}{2V_1} \qquad (6)$$

The results were obtained for interblade phase angles of 0, 90, and -90 deg. Positive interblade phase angle is defined such that airfoil N leads airfoil N + 1, etc. (refer to Fig. 6). Positive interblade phase angles would correspond to a wave moving in the direction of rotation in a rotor.

A typical airfoil displacement signal and the corresponding power spectrum are presented in Fig. 14. This signal was obtained from the optical displacement

meter while driving the airfoils at a frequency of 560 Hz. The power spectrum of the displacement signal, Fig. 14(b), indicates second and third harmonics with peak amplitudes at least 20 dB lower than the fundamental. A measure of the quality of the harmonic motion can be obtained from the power spectrum and expressed in terms of a harmonic distortion parameter as defined in (7). Analysis of the spectrum shown in Fig. 14(b) indicated that the harmonic distortion was about 2 percent through the second harmonic which is consistent with the results from the isolated airfoil experiment (7). If the third harmonic is considered, the distortion is about 7 percent.

The shock phase lag was determined by analyzing the high speed motion pictures of the images as they were reproduced by a photo-optical analyzer. As the airfoil passed through the maximum angle of attack, the lambda-shock continued to move downstream thus reaching its maximum position as the airfoil pitched downward. By observing several frames corresponding to this maximum position and correlating these frames with the angle of attack, a phase angle was determined. This phase angle, Φ_s, can be obtained from the difference between the time it takes the shock to reach its maximum position and the time the airfoil reaches the maximum angle of attack, or

$$\Phi_s = 2\pi f \, \Delta t \tag{7}$$

where

$$\Delta t = \frac{1}{2\pi f}\left[\cos^{-1}\left(\frac{\alpha_o - \alpha_m}{\bar{\alpha}}\right) - \cos^{-1}\left(\frac{\alpha_o - \alpha_s}{\bar{\alpha}}\right)\right] \tag{8}$$

The values of Φ_s determined in this manner do not necessarily represent the phase shift associated with the maximum shock strength. It was noted in (5) that the maximum shock strength is not reached at the maximum downstream position of the shock, but at some time later during its upstream motion. Therefore, the values of Φ_s obtained in this visual study of the flow could be lower than the phase lag based on maximum shock strength.

The resulting values of Φ_s are plotted as a function of the reduced frequency, Ω, in Fig. 15. All values of Φ_s were less than 80 deg; however, an appreciable amount of scatter is evident. The bars on each symbol represent the range of uncertainty in the maximum shock location resulting from the uncertainty in the instantaneous angle of attack of the airfoil. The straight-line least squares fit of the data presented in Fig. 15 indicates that the shock phase lag was greatest at the positive interblade phase angle test condition. The analysis presented in Appendix A indicates that the unsteady aerodynamic work per cycle is proportional to sin Φ_s (eq. (A17)); therefore, one might expect a greater contribution from the oscillating shock wave to the unsteady aerodynamic work for this case in which Φ_s is greatest. The analysis also suggests that for all of the observed values of Φ_s, the oscillating shock would contribute to stability rather than instability in the cascade.

Sequences from the motion pictures are shown in Fig. 16 for the three values of interblade phase angle and a nominal frequency of 550 Hz. By observing the progression of the shock with increasing time the sign of the interblade motion can readily be confirmed. Analysis of these images revealed a shock displacement of about 10 percent of the airfoil chord.

In order to examine the oscillating shock wave in more detail, another type of flow visualization experiment was performed in a pilot facility at the same frequency and velocity. In this experiment, rapid-double-pulse holography was used to observe the shock in three dimensions and thus determine the degree of spanwise deformation of the shock plane as the airfoils were oscillated. A highly twisted or three-dimensional shock could possibly explain some of the randomness in the observed shock phase lag results (Fig. 15) which were based on an analysis of Schlieren-type images. As the airfoils were oscillated a hologram was recorded and, after a preselected delay time, a second hologram was recorded on the same plate. In the reconstructed double image, interference fringes are formed because of the slight difference in the refractive index fields between the two exposures. Pulse delay times of 10 to 20 micro-seconds yielded the best images. The laser was randomly pulsed and up to 50 holograms were recorded.

A photograph of a typical reconstructed image is shown in Fig. 17. The suction surface shock wave is clearly evident. The degree of two-dimensionality appears to be good even though the end-wall boundary layers were relatively thick in this pilot facility. In some of the holograms, there appeared to be a spanwise variation in the fringe pattern. Since the formation and localization of that pattern depends upon the shock slope, curvature, and positional variation in shock strength, as well as the time variation of these quantities (11), there is some evidence for a spanwise variation in the space and time dependent properties of the shock wave. Although this observed variation in the fringe pattern is not yet fully understood, the results tend to support future work involving holographic observations of the flow in the present cascade.

CONCLUSIONS

The results of this investigation indicated that reasonably good steady-state periodicity could be obtained in a flutter cascade operating at near transonic velocities. Furthermore, the airfoils could be oscillated in this high speed environment to achieve frequencies believed to be consistent with the frequencies associated with transonic stall flutter in turbomachinery. Flow visualization methods, including Schlieren (or shadowgraph) and rapid-double-pulse holography, revealed some of the dynamic features of the lambda shock as the airfoils were oscillated in harmonic pitching motion. The shock phase lag based on an analysis of high speed motion pictures of Schlieren images was generally less than 80 deg. A linear fit of the results indicated that the greatest shock phase lag occurred at the positive interblade phase angle. An analysis of the effects of the oscillating shock on airfoil stability indicated that for all of the observed values of Φ_s, the oscillating shock would contribute to stability in the cascade. Future experiments involving holographic flow visualization and dynamic surface pressure measurements will be performed in order to better quantify the dynamic flow field.

REFERENCES

1. Carta, F. O., "Aeroelasticity and Unsteady Aerodynamics," The Aerodynamics of Aircraft Gas Turbine Engines, Oates, G. C., ed., AFAPL-TR-78-52, 1978, pp. 22-1 to 22-54.

2. Riffel, R. E. and Rothrock, M. D., "Experimental Determination of Unsteady Blade Element Aerodynamics in Cascades, Vol. 1: Torsional Mode Cascade," EDR-10119-Vol-1, Detroit Diesel Allison, Indianapolis, IN, June 1980 (NASA CR-159831).

3. Riffel, R. E. and Rothrock, M. D., "Experimental Determination of Unsteady Blade Element Aerodynamics in Cascades, Vol. II: Translation Mode Cascade," EDR-10361-Vol-2, Detroit Diesel Allison, Indianapolis, IN, Dec. 1980 (NASA CR-165166).

4. Carta, F. O. and St. Hilaire, A. O., "An Experimental Study on the Aerodynamic Response of a Subsonic Cascade Oscillating Near Stall," R76-912270, United Technologies Research Center, East Hartford, CT.

5. Tijdeman, H. and Seebass, R., "Transonic Flow Past Oscillating Airfoils," Annual Review of Fluid Mechanics, Vol. 12, M. Van Dyke, ed., Annual Reviews, Inc., Palo Alto, CA, 1980, pp. 181-222.

6. McCroskey, W. J. and Pucci, S. L., "Viscous-Inviscid Interaction on Oscillating Airfoils in Subsonic Flow," AIAA Paper 81-0051, Jan. 1981.

7. Boldman, D. R. and Buggele, A. E., "Wind Tunnel Tests of a Blade Subjected to Midchord Torsional Oscillation at High Subsonic Stall Flutter Conditions," NASA TM-78998, 1978.

8. Goldstein, M. E., Braun, W., and Adamczyk, J. J., "Unsteady Flow in a Supersonic Cascade with Strong In-passage Shocks," Journal of Fluid Mechanics, Vol. 83, Dec. 1977, pp. 569-604.

9. Dudzinski, T. J. and Krause, L. N., "Flow-Direction Measurement with Fixed-position Probes," NASA TMX-1904, 1969.

10. Lieblein, S., "Experimental Flow in Two-Dimensional Cascades," Aerodynamic Design of Axial-Flow Compressors, NASA SP-36, 1965, pp. 183-226.

11. Decker, A. J., "Fringe Localization Requirement for Three-Dimensional Flow Visualization of Shock Waves in Diffuse-Illumination, Double-Pulse Holographic Interferometry," NASA TP-1868, 1981.

APPENDIX A

DISCUSSION OF THE CONTRIBUTION OF THE OSCILLATING SHOCK TO AIRFOIL STABILITY

The unsteady aerodynamic work per cycle of oscillatory pitching motion can be expressed as

$$W = \oint \mathcal{R}e\mathcal{M} \cdot \mathcal{R}e\, d\alpha = \int_0^{2\pi} \mathcal{R}e\mathcal{M} \cdot \mathcal{R}e \frac{d\alpha}{d(\omega t)}\, d(\omega t) \tag{A1}$$

where $\mathcal{R}e\mathcal{M}$ and $\mathcal{R}e\,\frac{d\alpha}{d(\omega t)}$ represent the real parts of the moment and change in pitch angle, respectively. The moment in (A1) is obtained by integrating the product of the time-dependent pressures and corresponding moment arm over the surface of the airfoil, i.e.,

$$\mathcal{M}(t) = \int_0^C \left[P_l(x,t) - P_u(x,t)\right]\left(\frac{C}{2} - x\right)dx \tag{A2}$$

where the subscripts l and u denote the lower and upper surfaces of the airfoil, respectively. Now consider an oscillating airfoil with a normal shock on the upper (suction) surface as shown in the following sketch:

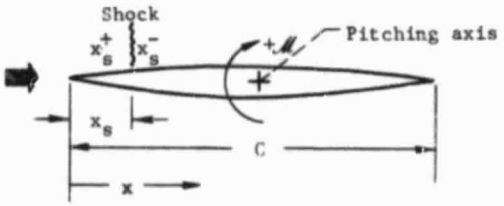

The contribution of the oscillating shock to the unsteady aerodynamic work for the case shown will depend on the forces on the upper surface where the shock is located. Therefore, (A2) can be simplified to give

$$\mathcal{M}(t) = -\int_0^C P_u(x,t)\left(\frac{C}{2} - x\right)dx \tag{A3}$$

Introducing the shock position coordinates, x_s^+ and x_s^- as shown in the sketch, the moment can be rewritten as

$$\mathcal{M}(t) = -\int_0^{x_s^+} P_u\left(\frac{C}{2} - x\right)dx - \int_{x_s^-}^C P_u\left(\frac{C}{2} - x\right)dx \tag{A4}$$

where $x_s^+ = \bar{x}_s^+ + \tilde{x}_s^+$ and

$$x^- = \bar{x}^- + \tilde{x}^- \tag{A5}$$

The values of $\bar{x}$ and $\tilde{x}$ represent the mean and unsteady perturbation components of shock position, respectively. Equation (A4) can be expanded to give

$$\mathcal{M}(t) = -\left[\int_0^{\bar{x}_s^+} P_u\left(\frac{C}{2} - x\right)dx + \int_{\bar{x}_s^+}^{\bar{x}_s^+ + \tilde{x}_s^+} P_u\left(\frac{C}{2} - x\right)dx - \int_{\bar{x}_s^-}^{\bar{x}_s^+ + \tilde{x}_s^+} P_u\left(\frac{C}{2} - x\right)dx + \int_{\bar{x}_s^-}^{C} P_u\left(\frac{C}{2} - x\right)dx\right] \tag{A6}$$

The moment associated with the shock motion is simply

$$\mathcal{M}_s(t) = -\int_{\bar{x}_s^+}^{\bar{x}_s^+ + \tilde{x}_s^+} P_u\left(\frac{C}{2} - x\right)dx + \int_{\bar{x}_s^-}^{\bar{x}_s^- + \tilde{x}_s^-} P_u\left(\frac{C}{2} - x\right)dx \tag{A7}$$

Let

$$P_u\left(\frac{C}{2} - x\right) = f(\bar{x}_s + \tilde{x}_s) \tag{A8}$$

Expanding the right side of (A8) in a Taylor's series centered at $\bar{x}_s$, we obtain

$$f(\bar{x}_s + \tilde{x}_s) = f(\bar{x}_s) + \left.\frac{\partial f}{\partial x}\right|_{x=\bar{x}_s} \cdot \tilde{x} + \cdots \tag{A9}$$

Consequently,

$$\mathcal{M}_s(t) = -\int_{\bar{x}_s^+}^{\bar{x}_s^+ + \tilde{x}_s^+} f(\bar{x}_s^+)dx - \int_{\bar{x}_s^+}^{\bar{x}_s^+ + \tilde{x}_s^+} \left.\frac{\partial f}{\partial x}\right|_{x=\bar{x}_s^+} \cdot \tilde{x}_s^+\, dx + \int_{\bar{x}_s^-}^{\bar{x}_s^- + \tilde{x}_s^-} f(\bar{x}_s^-)dx + \int_{\bar{x}_s^-}^{\bar{x}_s^- + \tilde{x}_s^-} \left.\frac{\partial f}{\partial x}\right|_{x=\bar{x}_s^-} \cdot \tilde{x}_s^-\, dx \tag{A10}$$

Upon integrating (A10) and neglecting higher order terms in $\tilde{x}_s$, the shock induced moment can be expressed as

$$\mathcal{M}_s(t) = -f(\bar{x}_s^+)\tilde{x}^+ + f(\bar{x}_s^-)\tilde{x}_s^- \qquad (A11)$$

If we assume $\tilde{x}^+ = \tilde{x}^-$ and $\bar{x}_s^+ = \bar{x}_s^- = \bar{x}_s$ the expression for the moment is

$$\mathcal{M}_s(t) = -\left[P_u\Big|^{\bar{x}_s^+}\left(\frac{C}{2} - \bar{x}_s\right) - P_u\Big|^{\bar{x}_s^-}\left(\frac{C}{2} - \bar{x}_s\right)\right]\tilde{x} \qquad (A12)$$

Assuming simple harmonic motion, the pitching angle and fluctuating shock position become

$$\alpha = \bar{\alpha}\, e^{i\omega t} \qquad (A13)$$

and

$$\tilde{x} = \overline{\Delta x}\, e^{i(\omega t - \phi_s)} \qquad (A14)$$

Introducing T, where $T = \omega t$ in (A1), the contribution to the aerodynamic work from the oscillating shock is

$$W_s = \int_0^{2\pi} \mathcal{R}e\,\mathcal{M}_s(t) \cdot \mathcal{R}e\,\frac{d\alpha}{dT}\,dT \qquad (A15)$$

or

$$W_s = -\left[P_u\Big|^{\bar{x}_s^+}\left(\frac{C}{2} - \bar{x}_s\right) - P_u\Big|^{\bar{x}_s^-}\left(\frac{C}{2} - \bar{x}_s\right)\right]\int_0^{2\pi} \mathcal{R}e\,\tilde{x} \cdot \mathcal{R}e\,\frac{d\alpha}{dT}\,dT \qquad (A16)$$

Integration of the right side of (A16) gives the following expression for the unsteady aerodynamic work due to shock motion:

$$W_s = \left(P_u\Big|^{\bar{x}_s^+} - P_u\Big|^{\bar{x}_s^-}\right)\left(\frac{C}{2} - \bar{x}_s\right)\overline{\Delta x}\;\bar{\alpha}\,\pi \sin\phi_s \qquad (A17)$$

The phase angle ϕ_s is the angle in which the shock wave lags the motion of the airfoil. The pressure difference across the shock always has a negative value whereas the shock displacement and pitching angle magnitudes are always positive. Therefore, by considering the sign of the term involving the mean position of the shock $\left(\frac{C}{2} - \bar{x}\right)$ and its phase lag ϕ_s, the following conclusions can be made for airfoils pitching about the midchord position.

Case I - Shock upstream of midchord and lagging the airfoil motion by 0 to 180 deg:

W_s is negative (contributes to airfoil stability)

Case II - Shock upstream of midchord and leading the airfoil motion by 0 to 180 deg:

W_s is positive (contributes to airfoil instability)

Case III - Shock downstream of the midchord and lagging the airfoil motion by 0 to 180 deg:

W_s is positive (contributes to airfoil instability)

Case IV - Shock downstream of the midchord and leading the airfoil motion by 0 to 180 deg:

W_s is negative (contributes to airfoil stability)

Based on the above considerations, the measured shock phase lag of $0 < \phi_s < 80$ deg obtained in this study implies that the oscillating shock on the airfoils contributes favorably to the stability of the cascade.

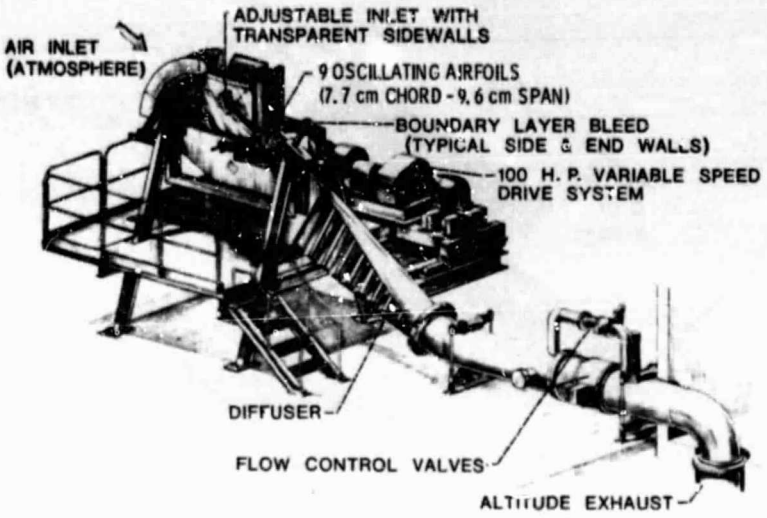

Figure 1. - Transonic oscillating cascade.

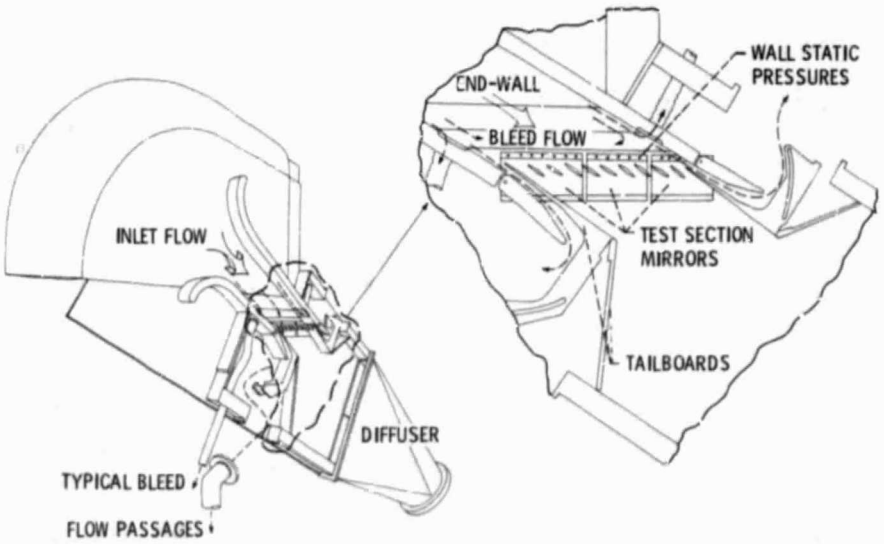

Figure 2. - Test section.

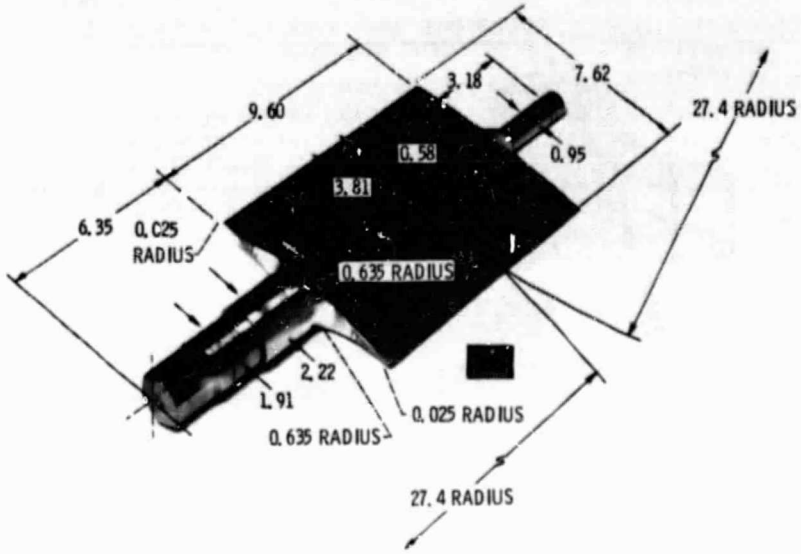

Figure 3. - Biconvex airfoil (all dimensions in centimeters).

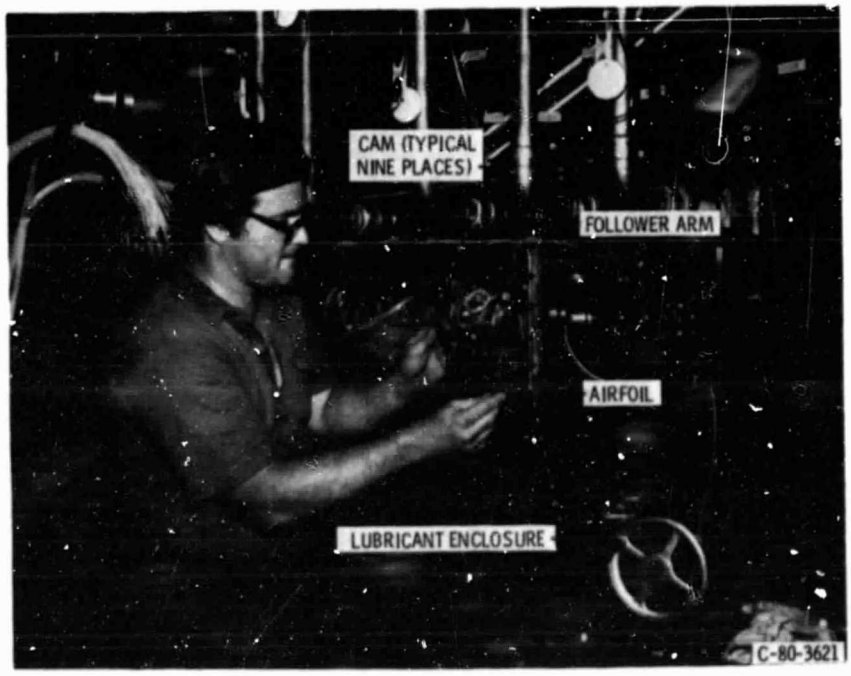

Figure 4. - Airfoil drive mechanism.

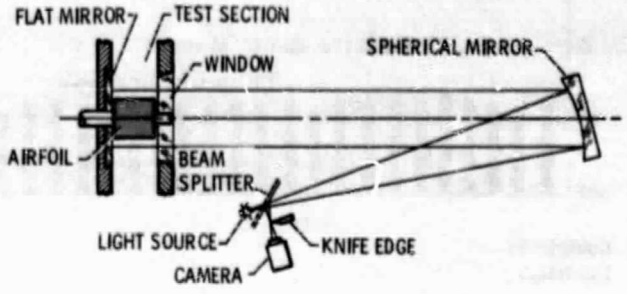

Figure 5. - Double-pass Schlieren system.

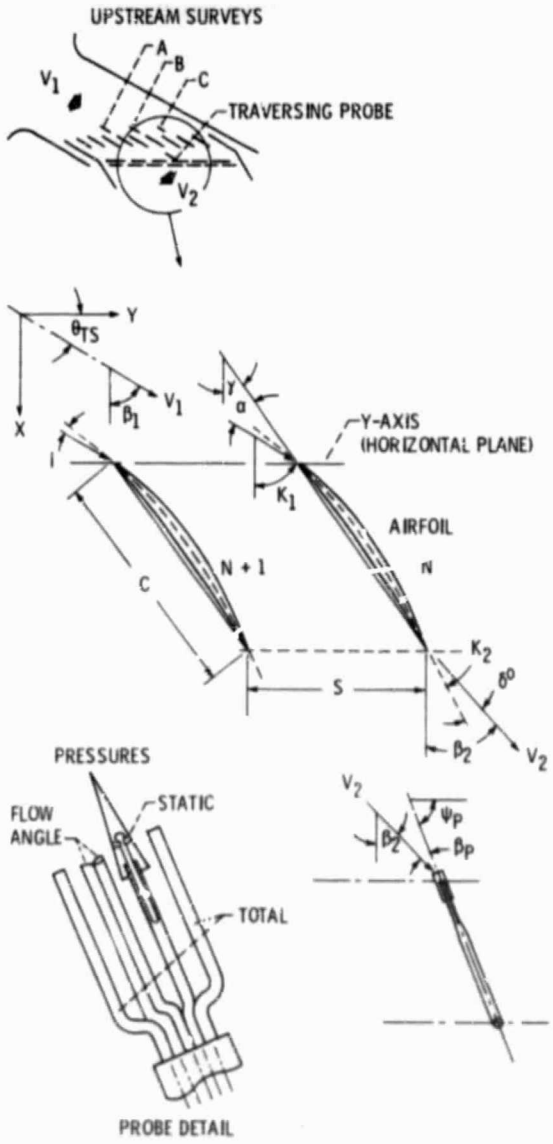

Figure 6. - Coordinate system and geometric parameters.

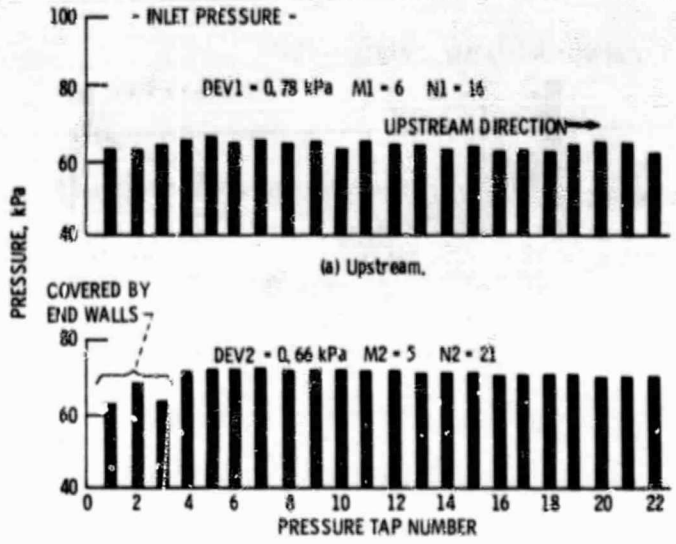

Figure 7. - End wall static pressure distributions.

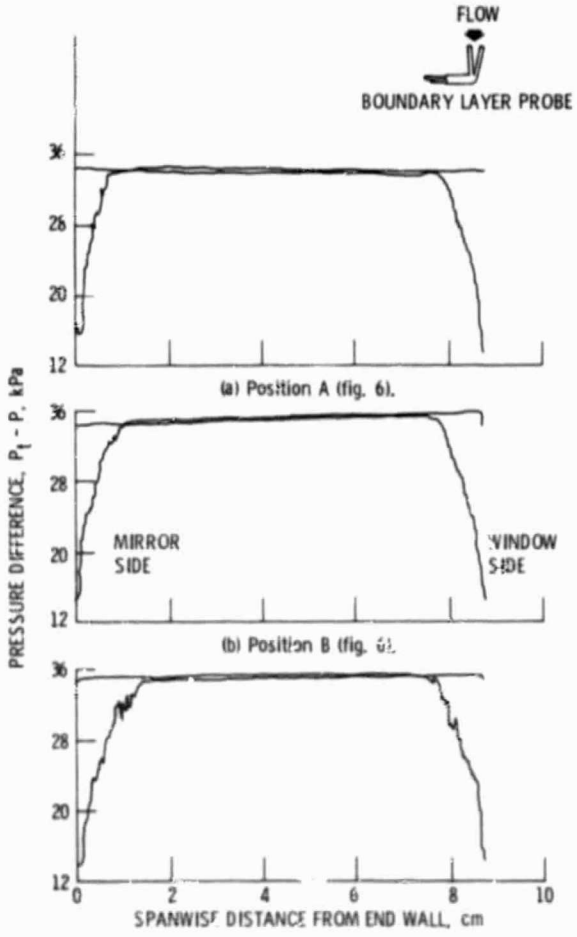

Figure 8. - Inlet end wall boundary layers at three tangential stations.

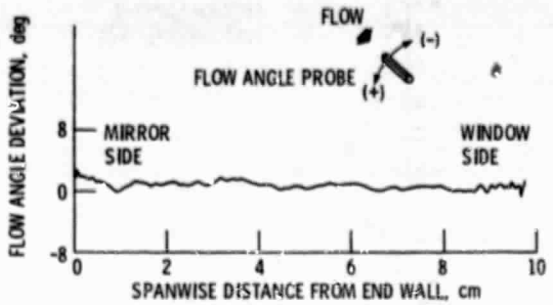

Figure 9. - Spanwise variation of inlet flow angle at center of cascade.

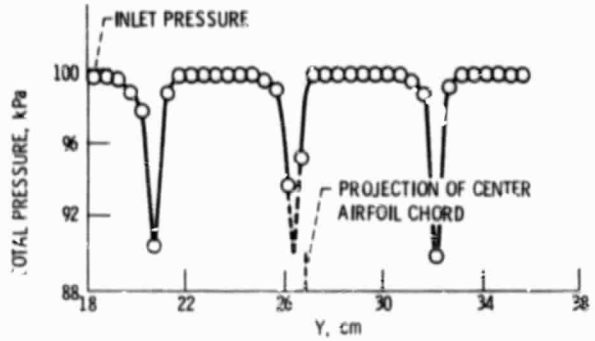

Figure 10. - Exit total pressure distribution across three passages.

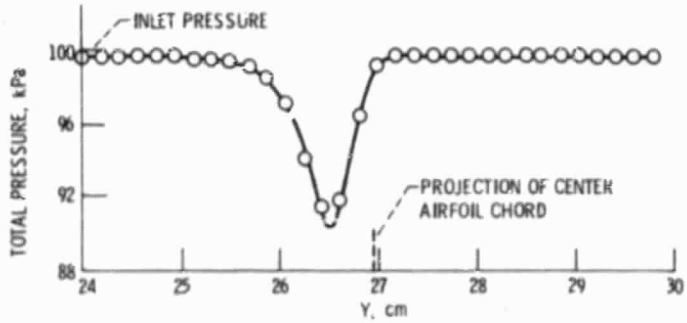

Figure 11. - Exit total pressure distribution across one passage.

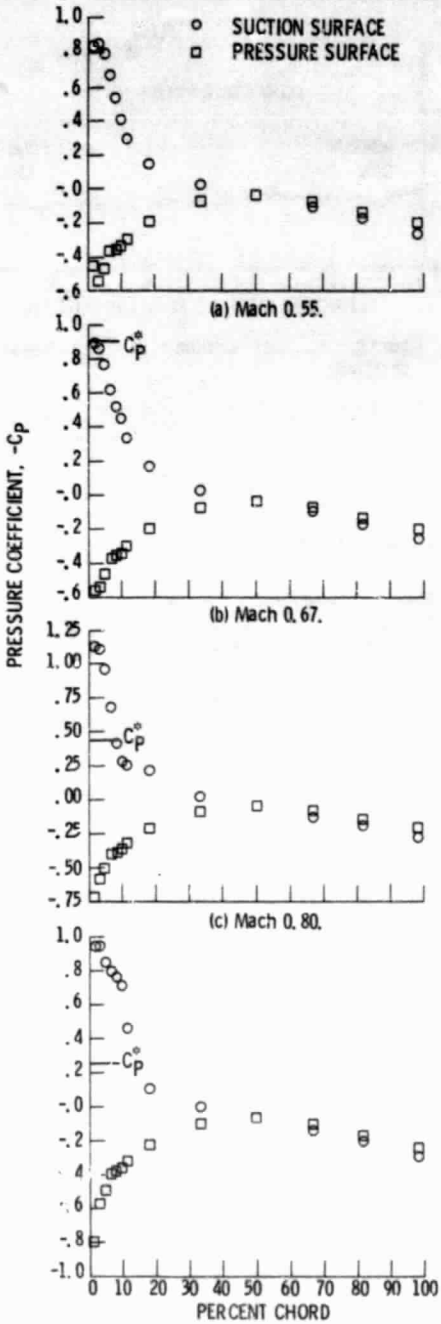

Figure 12. - Steady-state static pressure distributions on center airfoil.

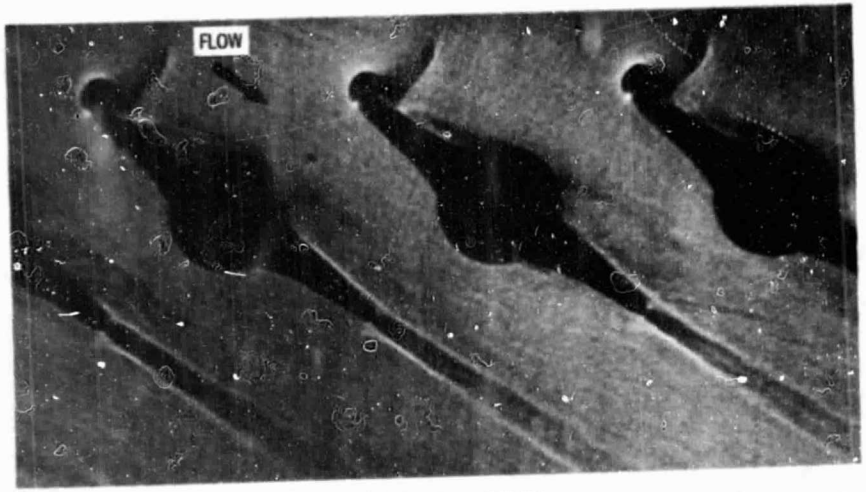

(a) DEFOCUSED SCHLIEREN.

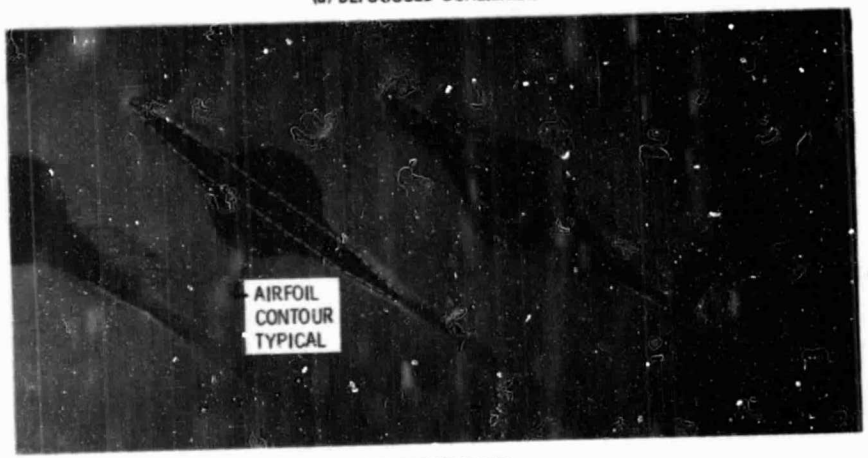

(b) BI-COLOR FILTER.

Figure 13. - Schlieren images of steady state flow, $M_1 = 0.80$.

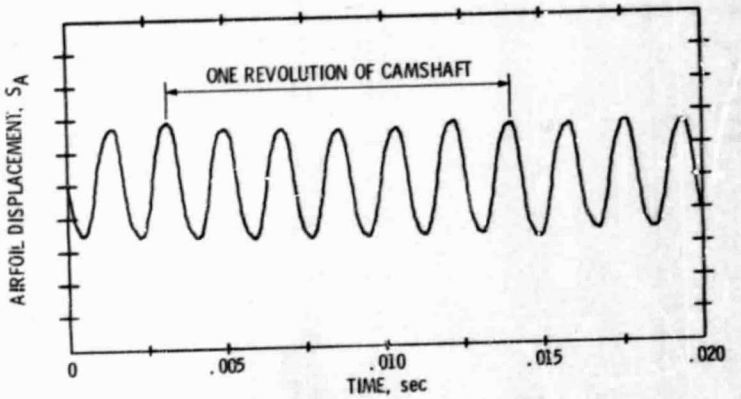

(a) Displacement signal for center airfoil.

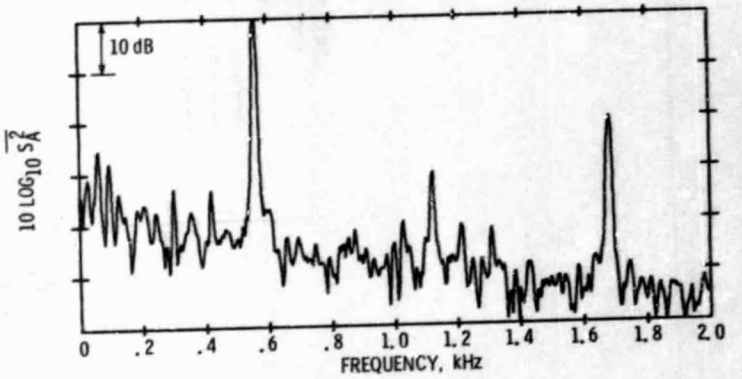

(b) Power spectrum of displacement signal.

Figure 14. - Typical center airfoil displacement signal and corresponding power spectrum, f = 560 Hz.

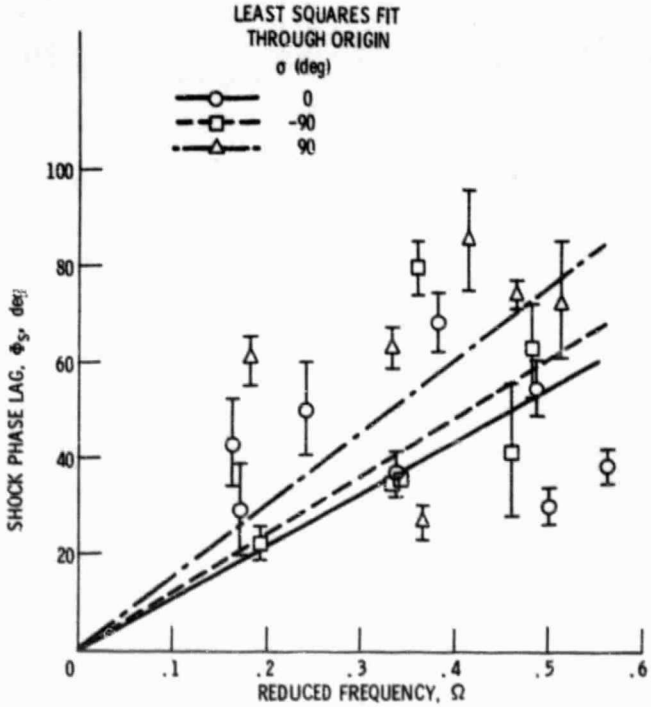

Figure 15. - Shock phase lag based on an analysis of high-speed motion pictures $M_1 = 0.80$.

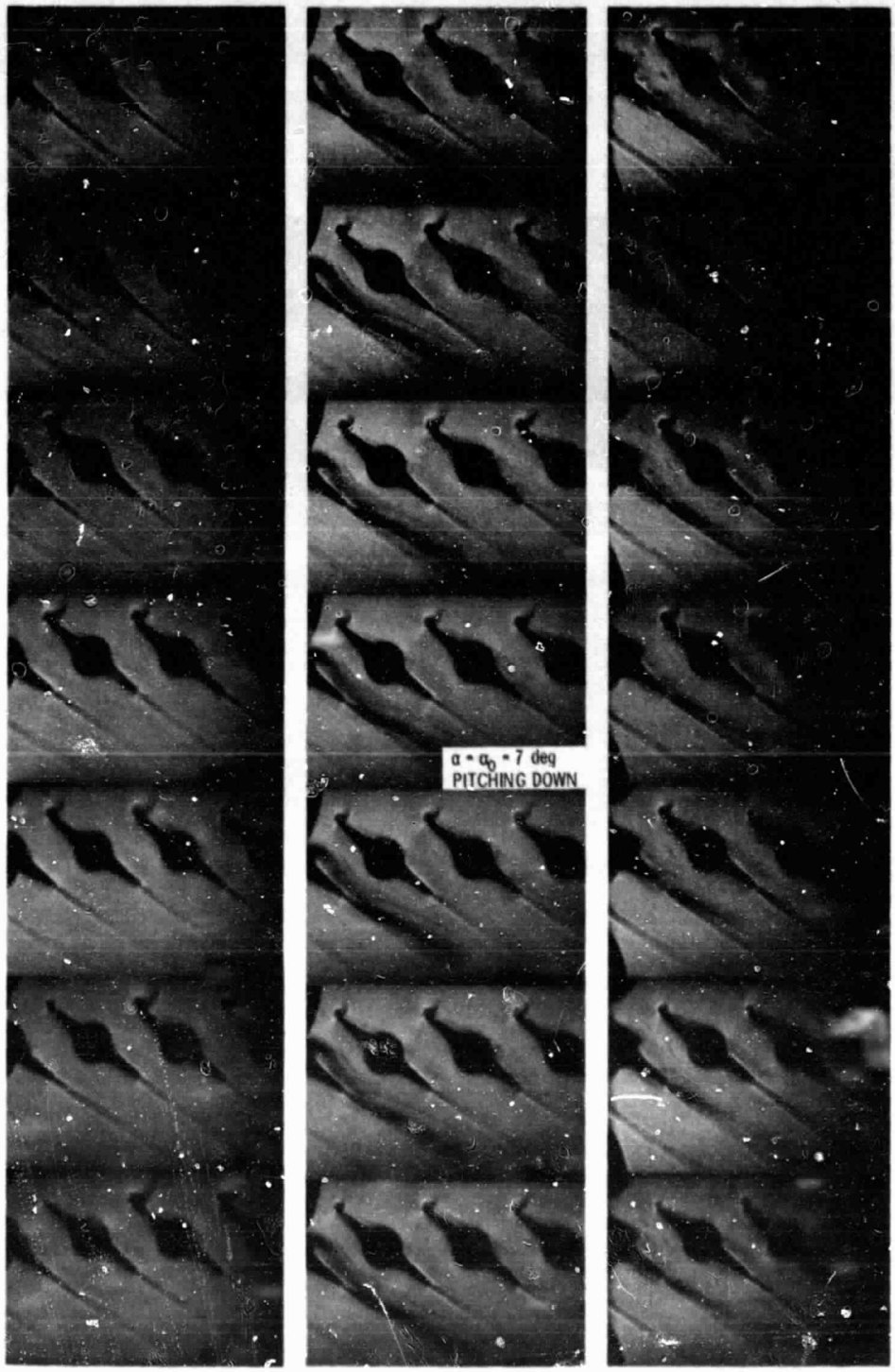

Figure 16. - Film sequences of oscillating airfoils at various interblade phase angles M = 0.80, 550 Hz.

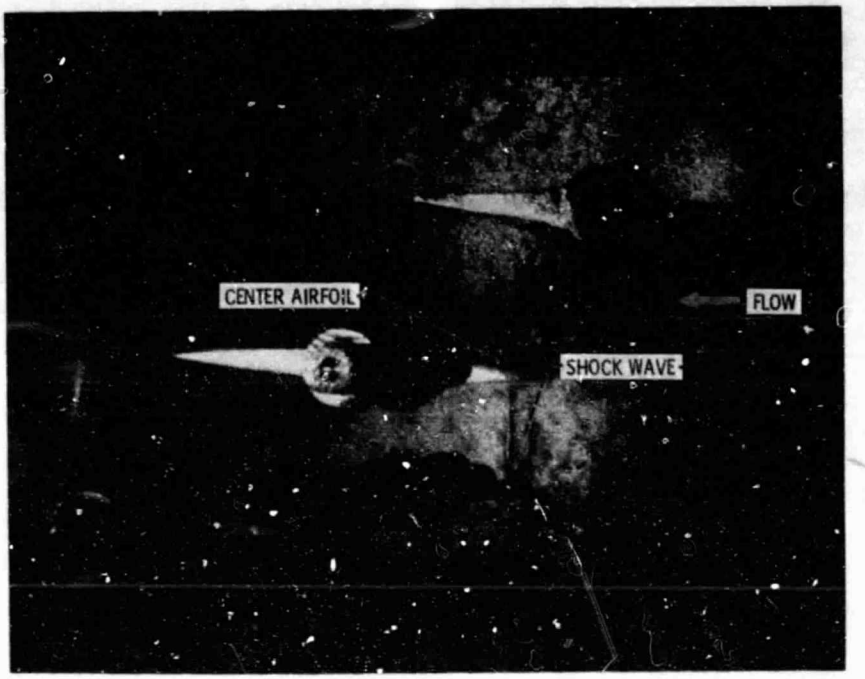

Figure 17. - Holographic fringe pattern of one state of a shock wave during oscillation at 580 Hz.